Materials Today Chemistry 46 (2025) 102795

Contents lists available at ScienceDirect

Materials Today Chemistry

journal homepage: www.journals.elsevier.com/materials-today-chemistry/

Structural design and functionalization of benzoxazine-modified octavinylsilsesquioxane hybrid porous polymer through Sonogashira coupling reaction

Ching-Wen Hsiao, Mohamed Gamal Mohamed, Shiao-Wei Kuo *

Department of Materials and Optoelectronic Science, Center of Crystal Research, National Sun Yat-Sen University, Kaohsiung, 804, Taiwan

ARTICLE INFO

Keywords:
Octavinylsilsesquioxane
Benzoxazine
Sonogashira–Hagihara coupling
Hybrid porous polymer
Ring-opening polymerization
CO_2 adsorption

ABSTRACT

In this work, we present the synthesis of a new hybrid porous polymer (HPP) using octavinylsilsesquioxane (OAVS), as a rigid and multifunctional core. The OAVS was functionalized with a 4-bromostyrene unit to create the OAVS-8Br monomer, which was subsequently used to generate the OAVS-BZ HPP through the Sonogashira–Hagihara coupling reaction with a benzoxazine-based monomer of DHTA-EA-BZ. The resulting OAVS-BZ HPP displayed the specific surface area of 43.5 $m^2\ g^{-1}$ and a total pore volume of 0.17 $cm^3\ g^{-1}$, indicative of its microporous nature. Most importantly, the OAVS-BZ HPP integrated many functional groups, including the vinyl (C═C), alkyne (C ≡C), benzoxazine (BZ) unit, and a rigid POSS framework; the resulting materials exhibit enhanced chemical versatility, structural rigidity, and the potential for extended π-conjugation. Thermal ring-opening polymerization (ROP) of the OAVS-BZ HPP led to solid-state structural transformations, which were monitored using DSC, FTIR, and NMR, revealing the emergence of Mannich bridge structures and phenolic OH groups. Although the thermal ROP did not significantly enhance the overall network structure and the specific BET surface area (SA_{BET}) decreased to 21.2 $m^2\ g^{-1}$, additional reaction sites were added, thereby improving the gas adsorption performance. Notably, the CO_2 adsorption capacity increased from 16.0 to 23.1 $cm^3\ g^{-1}$ (STP) under 1 bar and 298 K after thermal ROP. This enhancement is attributed to incorporating phenolic OH and Mannich bridge functional groups, which provide additional active sites for CO_2 adsorption. Overall, this study demonstrates the potential of OAVS-based hybrid porous polymers for CO_2 capture and highlights the impact of solid-state chemical transformations on the gas adsorption properties.

1. Introduction

In an era of ever-increasing innovation, structural design of advanced materials is crucial for achieving enhanced performance in various applications. Hybrid polymer porous materials (HPPs) typically possess a high specific surface area and a diverse pore size distribution, which enables them to exhibit remarkable effectiveness in energy storage, adsorption, catalysis, and separation processes [1–14]. By using synthetic methods (such as Heck reaction, Sonogashira Coupling, Suzuki reaction, etc.), the structure, pore size, and surface properties can be finely controlled to fulfill the demands of various applications [15–22]. Since HPP combines organic and inorganic components, different functional groups, such as aromatic rings, amine, and hydroxyl OH groups, could be introduced according to needs, thus giving the material a variety of chemical reactivity and selectivity.

In many previous studies [23–32], octavinylsilsesquioxane (OAVS) has emerged as a promising molecular cage because of its well-defined three-dimensional structure, high thermal stability, and has been widely employed in the synthesis of HPP. Cheng et al. expanded and refined the structure of OAVS through various synthetic methods, enhancing its applicability by introducing diverse terminal functional groups [33]. Chaikittisilp et al. synthesized an HPP with a high specific surface area by employing OAVS functionalized with a terminal bromine group [34]. Building on the inherent advantages of HPP, numerous studies have enhanced their functionality by incorporating specific functional groups. Among these, the benzoxazine (BZ) group has garnered substantial attention as a result of its excellent thermal stability, low flammability, high char yield, and versatile chemical reactivity [35–47]. However, traditional polybenzoxazine (PBZ) usually suffers from limited porosity, which restricts the potential application in

* Corresponding author.
E-mail address: kuosw@facutly.nsysu.edu.tw (S.-W. Kuo).

https://doi.org/10.1016/j.mtchem.2025.102795
Received 3 March 2025; Received in revised form 6 May 2025; Accepted 29 May 2025
Available online 31 May 2025

the field requiring high surface areas, such as catalysis and adsorption. In our previous studies [36,37,39,44,48], incorporating BZ into the porous structure has provided additional cross-linking sites through thermal ring-opening polymerization (ROP), which usually uses an organic building block that results in relatively lower thermal stability. In this study, the incorporation of OAVS into PBZ networks presents an innovative approach to overcoming these limitations, enabling the development of inorganic hybrid porous materials with enhanced structural and thermal properties.

Heck reaction is the most convenient and easy approach to synthesize the highly stable HPP containing OAVS compound by using multi-functionalized bromine aromatic rings with C═C unit from OAVS by palladium-catalyzed cross-coupling reaction [49–53]. However, the Heck reaction usually requires high reaction temperatures (>120 °C), which may lead to undesirable side reactions, such as benzoxazine ring-opening or polymer degradation to form OAVS-BZ HPP. The Sonogashira coupling reaction is also used in palladium-catalyzed cross-coupling reactions for forming C≡C bonds, but they have distinct mechanisms and advantages compared with the Heck reaction. The Sonogashira reaction occurs under milder conditions (90 °C), minimizing the risk of side reactions and preserving the integrity of the benzoxazine ring. This makes it especially suitable for systems containing thermally sensitive structures such as the benzoxazine moiety. In addition, the Sonogashira coupling introduces a conjugated alkyne linker, which enhances electronic delocalization within the polymeric network with a more robust, cross-linked network. While other palladium-catalyzed coupling reactions like the Suzuki coupling (involving organoboron reagents) are also known for their functional group tolerance and relatively mild conditions, Sonogashira coupling was chosen here due to its superior ability to preserve benzoxazine ring integrity and its capacity to introduce rigid, conjugated linkers that benefit the resulting polymer's electronic properties and structural stability.

To achieve the OAVS-BZ HPP, the terminal alkyne benzoxazine (DHTA-EA-BZ, Scheme 1(b) [36]) and OAVS functionalized with bromine (OAVS-8Br, Scheme 1(a)) were synthesized. We employed the Sonogashira coupling reaction to synthesize the OAVS-based hybrid porous polymer (OAVS-BZ HPP) by reactive OAVS-8Br and DHTA-EA-BZ, as shown in Scheme 1(c). The presence of bromine in OAVS-8Br facilitates efficient coupling with the triple bonds of the benzoxazine monomer, leading to the formation of a robust and highly cross-linked network. We can expect that this new OAVS-BZ HPP would include multiple functional groups such as vinyl groups (C═C), alkynes (C≡C), benzoxazine (BZ) units, and a rigid POSS framework to enhance chemical versatility, structural rigidity, and potential for extended π-conjugation with microporous structure. Because of benzoxazine units in OAVS-BZ HPP, after thermal ROP was performed to obtain poly (OAVS-BZ) HPP and although this procedure did not enhance the overall network structure, it provides the additional reactive sites such as phenolic OH groups and Mannich bridges, the resulting facilitate strong intermolecular hydrogen bonds and acid/base interactions with CO_2 gas molecules, thereby enhancing the material's gas absorption capacity [36,37,54–57]. By combining the advantages of OAVS and benzoxazine chemistry, this work aims to develop a new class of hybrid porous polymers with high thermal stability and tunable porosity. This finding contributes to the growing field of high-performance porous organic polymers and provides valuable insights into the design of functional porous networks for advanced applications.

2. Experimental section

2.1. Materials

N, N-dimethylacetamide (DMAc), and N,N-dimethylformamide (DMF) were obtained from Alfa Aesar. Octavinylsilsesquioxane (OAVS), 4-bromostyrene, Grubbs catalyst, dichloromethane (DCM), sodium borohydride ($NaBH_4$), copper(I) iodide (CuI), triphenylphosphine (PPh_3), tetrakis(triphenylphosphine)palladium(0) [$Pd(PPh_3)_4$], triethylamine (Et_3N), paraformaldehyde $(CH_2O)_n$, 4-ethynylaniline (EA), 2,5-dihydroxyterephthalaldehyde (DHTA), and potassium carbonate (K_2CO_3) were purchased from Sigma-Aldrich. The synthesis of DHTA-EA-BZ monomer (Scheme 1(b)) was discussed in detail in our previous study [36].

2.2. The synthesis of OAVS-8Br monomer

Grubbs' catalyst (35.3 mg, 0.04 mmol), octavinylsilsesquioxane (OAVS, 632 mg, 1 mmol), and 4-bromostyrene (1.6 mL, 12 mmol) were added to a one-neck flask. DCM was used as a solvent. After performing three freeze-pump-thaw cycles under vacuum, the reaction solution was heated to 90 °C for 96 h under a nitrogen environment. After the reaction solution was concentrated, it was precipitated in MeOH, then filtered to get the solid. The powder was subjected to silica gel column chromatography (DCM/Hexane = 1/1) to obtain a white powder with a yield of ca. 80 wt%. FTIR (KBr, cm^{-1}): 3022 (C–H aromatic), 1607 (C═C), 1098 (Si–*O*–Si). ^{1}H NMR (DMSO-d_6, ppm, Fig. S1): δ = 6.5 (Si–C–H), 7.3 (C═C–H), 7.5–7.6 (aromatic protons). ^{13}C NMR ($CDCl_3$, ppm): δ = 117.9 (C═C), 123.2 (Si–C), 128.3–148.1 (aromatic carbons). ^{29}Si NMR ($CDCl_3$, ppm): δ = −81.1 (Si–*O*–Si)

2.3. The synthesis of OAVS-BZ hybrid porous polymer (HPP)

OAVS-8Br (240 mg, 1 mmol), $Pd(PPh_3)_4$ (35 mg), DHTA-EA-BZ (200 mg, 4 mmol), CuI (5 mg, 0.2 mmol), and PPh_3 (6.7 mg, 0.2 mmol) were

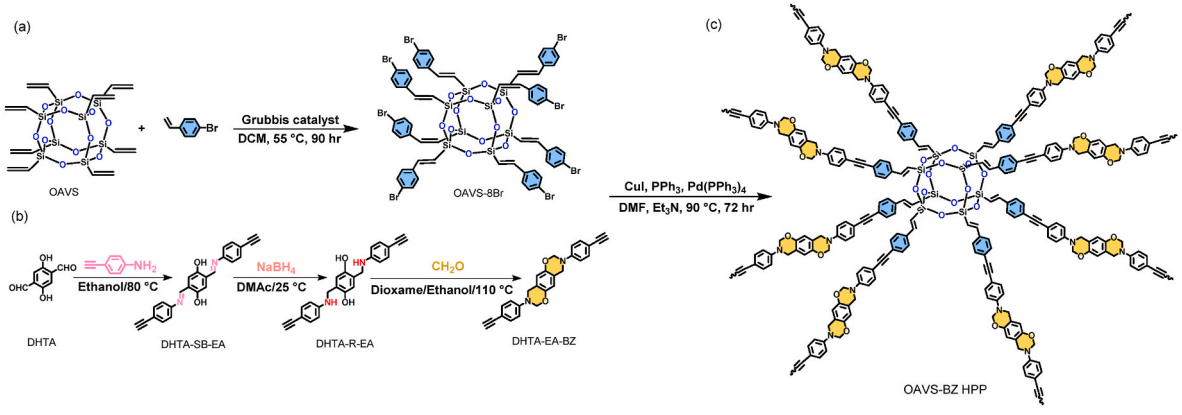

Scheme 1. The synthesis of (a) OAVS-8Br based on OAVS through olefin metathesis reaction, (b) DHTA-EA-BZ from DHTA, and (c) OAVS-BZ HPP through Sonogashira coupling reaction.

added to a one-neck flask. DMF and Et_3N were used as the solvents. The reaction was implemented in a nitrogen environment at 90 °C for 3 days. After the solid was washed several times with DMF, THF, MeOH, and acetone, it was dried in the oven for 2 days, yielding a brown powder. Yield (50 %).

3. Results and discussion

3.1. Synthesis of OAVS-8Br

To explore the synthesis and functionalization of novel hybrid porous polymer (HPP) based on POSS nanoparticle, we used multifunctional octavinylsilsesquioxane (OAVS) compound as the core structure. It possesses inherent rigidity, precise geometry, and remarkable adaptability, enhancing its synthetic versatility. Initially, we synthesized OAVS-8Br through an olefin metathesis reaction using OAVS, 4-bromostyrene, and the Grubbs catalyst [Scheme 1(a)].

After the reaction, the FTIR spectra of OAVS and OAVS-8Br, as shown in Fig. 1(a) revealed the characteristic peaks for the Si–*O*–Si unit (1098 cm^{-1}) and the C=C unit (1607 cm^{-1}). In addition, the aromatic C–H stretch was observed around 3022 $cm^{-1,}$ =became obvious after the formation of OAVS-8Br. To identify the chemical structure of OAVS-8Br, the ^{1}H NMR measurement was also conducted, as shown in Fig. 1 (b). The original Si–CH=CH characteristic peak of OAVS was found to have multiple peaks at 5.9–6.1 ppm, and it was shifted to 6.5 ppm (*a*) and 7.3 ppm (*b*) in OAVS-8Br, while an aromatic signal emerges at 7.8 ppm (*c, d*) following the attachment of 4-bromostyrene of OAVS-8Br monomer. We also observed that the ^{13}C NMR spectrum of OAVS-8Br monomer [Fig. 1(c)] reveals the distinct shifts compared to the original OAVS spectrum. The peaks at 136.8 ppm (*a*) and 128.3 ppm (*b*) were shifted to 123.2 ppm and 117.9 ppm, respectively, upon 4-bromostyrene incorporation. Additionally, the aromatic ring carbons are observed within the range of 128.3–148.1 ppm. Similarly, the ^{29}Si NMR spectra as displayed in Fig. 1(d) demonstrate that the Si–*O*–Si characteristic peak remains unchanged at −81.1 ppm before and after the reaction, indicating that the POSS cage structure was retained. All the spectra analyses indicate that the chemical structure of OAVS remained intact during the olefin metathesis process, and our OAVS-8Br was

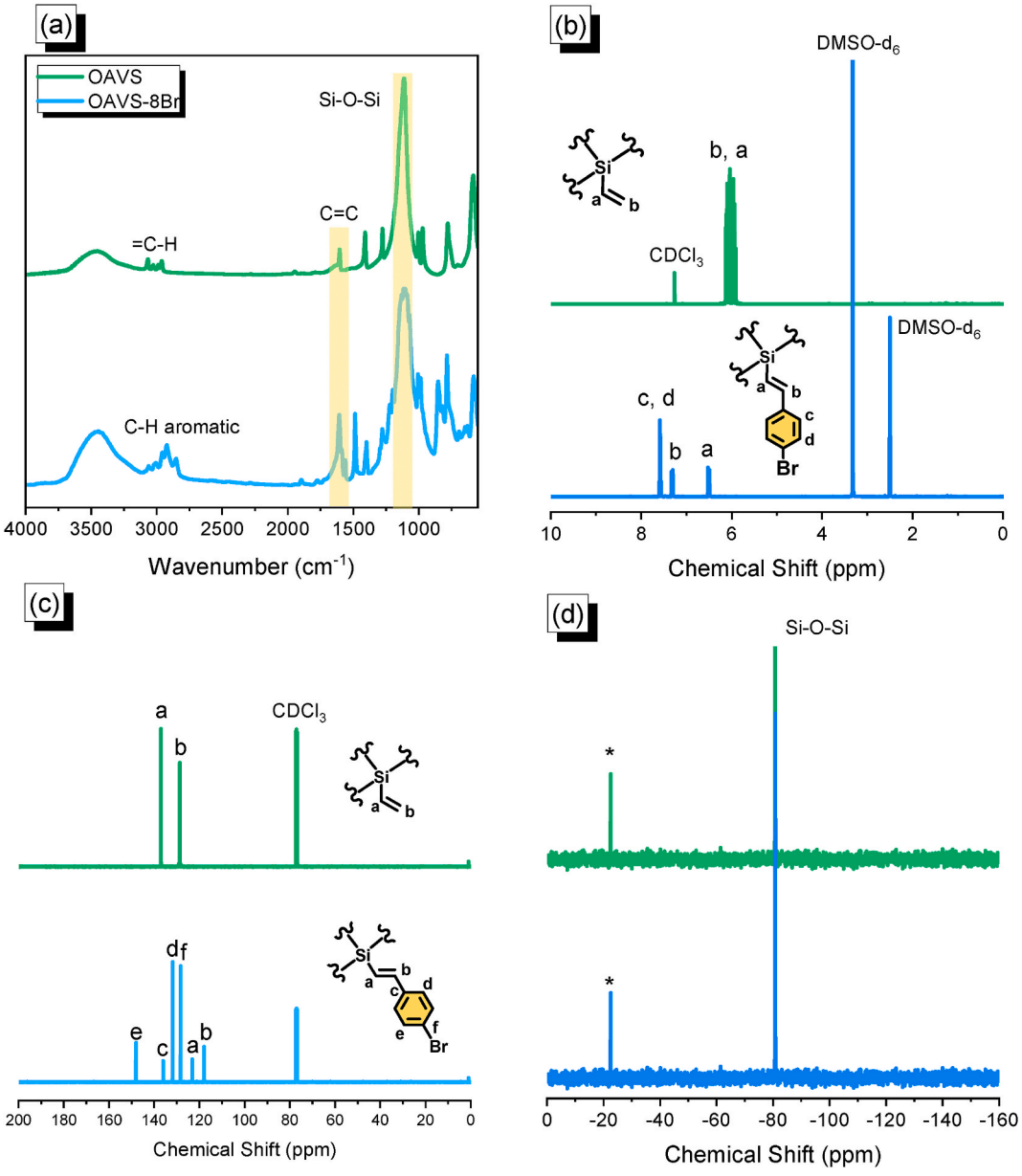

Fig. 1. (a) FTIR, (b) ^{1}H, (c) ^{13}C, and (d) ^{29}Si NMR spectra of OAVS and OAVS-8Br.

synthesized successfully. By reacting of OAVS with bromostyrene, a bromine-terminated functional group was introduced to OAVS, enabling further modification through the Suzuki or Sonogashira–Hagihara coupling reaction.

3.2. Synthesis of OAVS-BZ HPP

We synthesized OAVS-BZ HPP via the Sonogashira–Hagihara coupling reaction between OAVS-8Br and DHTA-EA-BZ as shown in Scheme 1(c) and [Fig. 2(a)]. FTIR and solid-state NMR spectroscopy, TGA, and DSC were employed to confirm the structural linkage and thermal behavior of OAVS-BZ HPP as presented in Fig. 2(b)-2(f). Firstly, Fig. 2(b) shows the FTIR spectrum of OAVS-BZ HPP, which confirms that the characteristic peaks for Si–*O*–Si unit from OAVS-8Br (1098 cm^{-1}), C≡C unit (2100 cm^{-1}), and the oxazine ring at 937 cm^{-1} from DHTA-EA-BZ remain unchanged after the Sonogashira–Hagihara coupling reaction. Most importantly, the C≡C–H peak at 3228 cm^{-1} from DHTA-EA-BZ disappeared in OAVS-BZ HPP, indicating the successful synthesis of OAVS-BZ HPP. The ^{13}C NMR of DHTA-EA-BZ and OAVS-8Br, and solid-state ^{13}C NMR spectrum of OAVS-BZ HPP, as shown in Fig. 2(d), exhibits a peak distribution consistent with its molecular structure. The characteristic peak for Si–**CH**=**CH$_2$** in OAVS-8Br, originally located at 117.2 ppm (*b*), was shifted to 99.5 ppm after the Sonogashira–Hagihara reaction, confirming the structural transformation. The emergence of the C≡C peak at 66.6 ppm (*a*) further verifies the successful attachment of DHTA-EA-BZ. Additionally, the characteristic peaks of the benzoxazine (BZ) group appear at 78.3 ppm (*e*) and 53.1 ppm (*f*). The dense and split peaks observed in the 120–150 ppm range correspond to aromatic carbons, confirming the incorporation of the benzene ring structure. Moreover, the solid-state ^{29}Si NMR spectrum (Fig. 2(e)) of OAVS-BZ HPP reveals a slight signal at ca. −81 ppm, indicating that the number of OAVS becomes fewer than expected. This result further supports the successful integration of DHTA-EA-BZ onto OAVS-8Br. In thermogravimetric analysis (TGA), as shown in Fig. 2(c), after the Sonogashira–Hagihara reaction, the thermal degradation temperature (T_{d10} = 411 °C) of OAVS-BZ HPP was located between DHTA-EA-BZ (T_{d10} = 346 °C) and OAVS-8Br (T_{d10} = 485 °C) as expected; however, the char yield of OAVS-BZ HPP (70.3 wt%) was both higher than the original DHTA-EA-BZ (62.1 wt%) and OAVS-8Br (67.9 wt%), due to highly network structure in this hybrid porous polymer, which were summarized in Table S1. Finally, the DSC analyses effectively demonstrate the connection of DHTA-EA-BZ while examining the thermal ring-opening polymerization behavior of OAVS-BZ HPP as shown in Fig. 2(f). The sharp exothermic thermal ROP peak of DHTA-EA-BZ is observed at 236 °C, with a reaction enthalpy of 290 J g^{-1}. After the Sonogashira–Hagihara coupling reaction, the endothermic peak becomes broad and shifts to 309 °C, and the enthalpy decreases to 168 J g^{-1}. This is due to the presence of the rigid and bulky OAVS structure, which limits molecular mobility and results in a more gradual thermal response. In addition, the formation of a network structure typically causes the exothermic peak to shift to a higher temperature, suggesting that the incorporation of OAVS into the HPP influences thermal ROP behavior by modulating the polymerization kinetics and decomposition pathway. Furthermore, a higher degree of cross-linking reduces the number of available active reaction sites, leading to a decrease in the total heat release.

To investigate the porous characteristics of the OAVS-BZ HPP, the N_2 adsorption/desorption isotherm at 77 K was utilized to analyze, as displayed in Fig. 3(a). The OAVS-BZ HPP could be classified as type I according to the IUPAC definition and the SA_{BET} of 43.5 m^2 $g^{-1,}$ with a Vtotal of 0.17 cm^3 $g^{-1,}$ and the average pore size is ca. 2.02 nm. Fig. 3(b) displays the X-ray diffraction pattern analyses of OAVS-8Br and OAVS-BZ HPP, where the OAVS-8Br shows multiple clear diffraction peaks, especially in the range of 5°–30°, indicating that the OAVS-8Br has

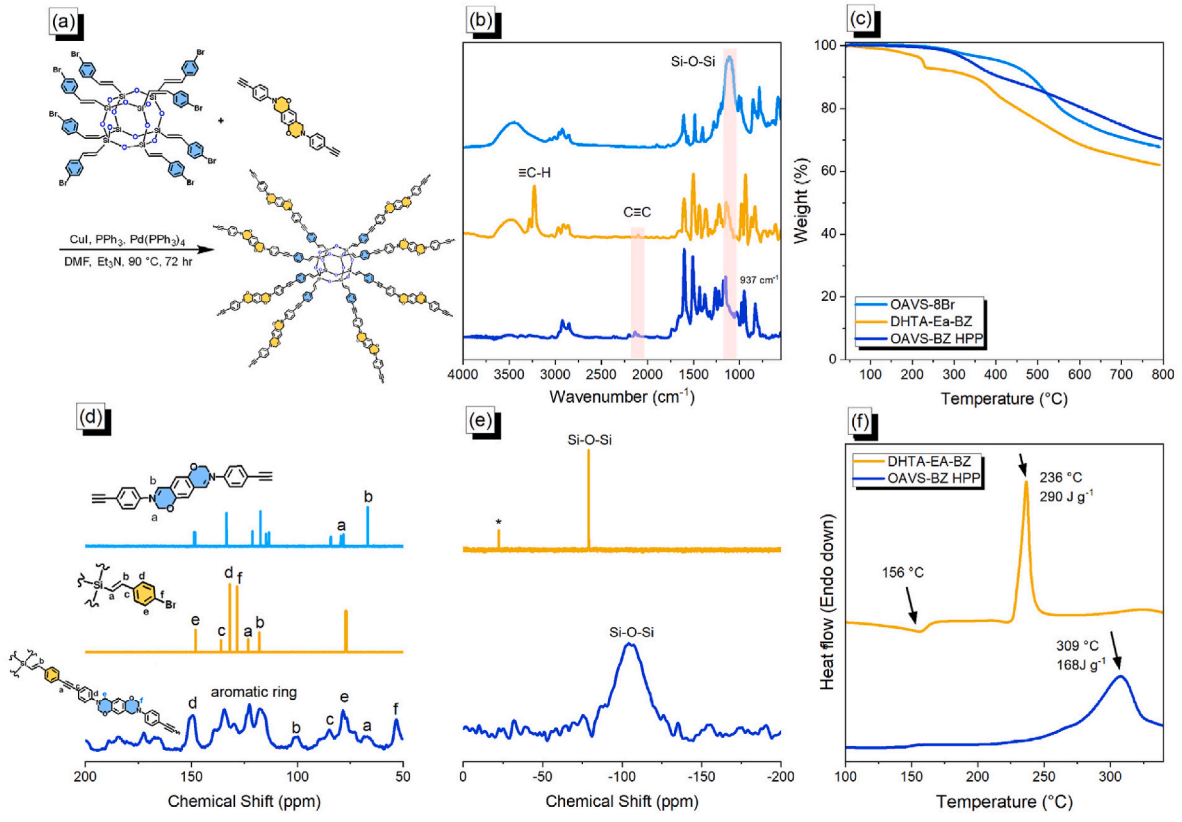

Fig. 2. (a) Synthesis of OAVS-BZ HPP from OAVS-8Br and DHTA-EA-BZ by using Sonogashira coupling reaction, and their corresponding (b) FTIR spectra, (c) TGA, (d–e) ^{13}C and ^{29}Si NMR solution and solid-state spectra, and (f) DSC analyses.

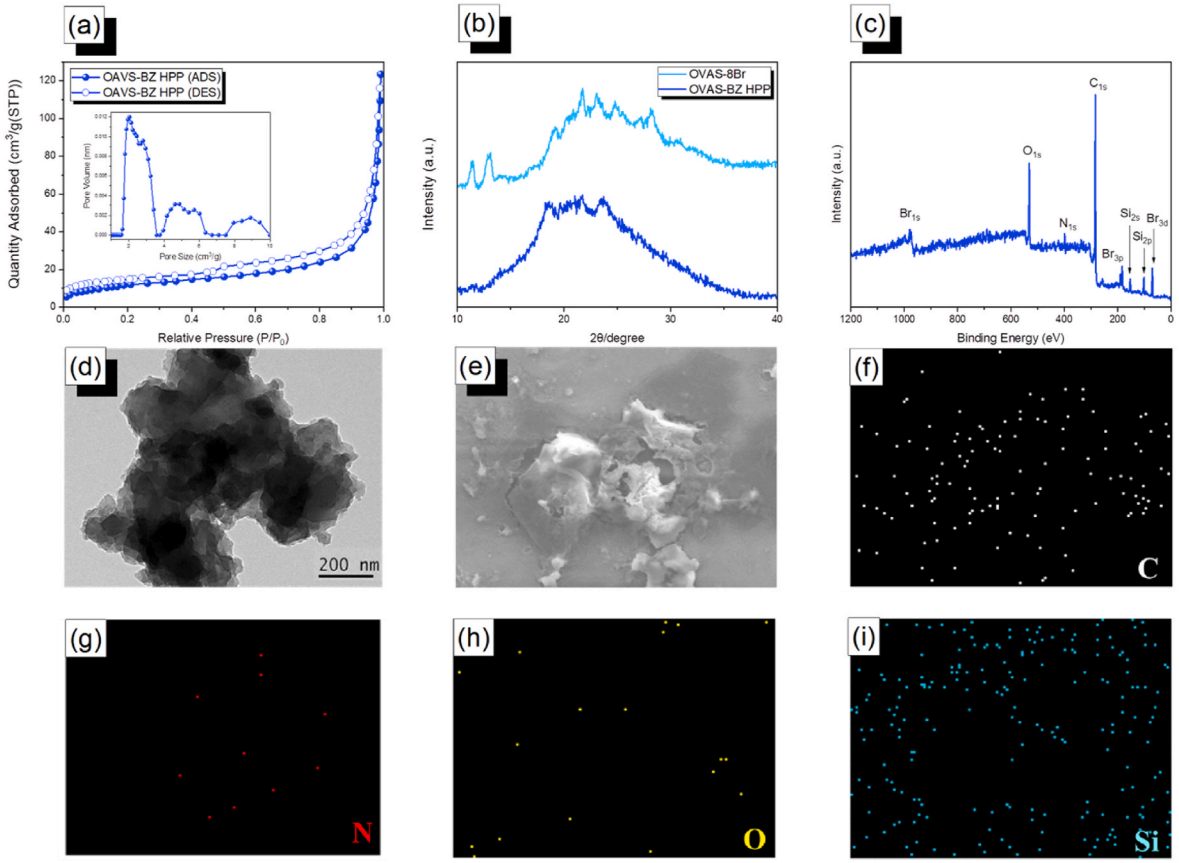

Fig. 3. (a) N_2 adsorption/desorption isotherms at 77 K and its corresponding pore size distribution of OAVS-BZ HPP, (b) Wide-angle X-ray diffraction patterns of OAVS-8Br and OAVS-BZ HPP and the corresponding (c) XPS spectrum, (d) TEM, (e) SEM, and SEM-EDS analyses of (f) C, (g) N, (h) O, and (i) Si atoms of OAVS-BZ HPP.

certain crystallinity based on its cubic molecular packing [58,59]. Furthermore, the XRD pattern of OAVS-BZ HPP becomes more blurred, with the main diffraction peak centered around 20°, indicating enhanced amorphous characteristics typical of a hybrid porous polymer.

Compared with OAVS-8Br, its overall structure may be more disordered, possibly due to polymer chemical reactions leading to structural destruction or reduced crystallinity. Transmission electron microscopy (TEM) and scanning electron microscopy (SEM) images of OAVS-BZ HPP were displayed in Fig. 3(d) and (e) and their corresponding elemental mappings for C, N, O, and Si, as well as energy dispersive X-ray (EDX) spectra as illustrated in Fig. 3(f)–(i). The TEM image (Fig. 3(d)) revealed that the OAVS-BZ HPP exhibited amorphous and disordered agglomerations. Fig. 3(e) shows the SEM image of OAVS-BZ HPP, suggesting a fragmented and dispersed morphology, and the EDX mapping (Fig. 3(f)–(i)) confirms that C, N, O, and Si atoms are evenly distributed throughout the sample. Further elemental analyses can also be confirmed from XPS results (Fig. 3(c)), and the compositions were summarized in Table S2. Based on all characterizations such as FTIR, NMR, DSC, TGA, N_2 adsorption/desorption, XRD, and XPS, the synthesis of OAVS-BZ HPP with porous structure and high thermal stability behavior was successfully achieved in this study.

3.3. Thermal ring-opening polymerization of OAVS-BZ HPP

We performed thermal ROP of OAVS-BZ HPP to form solid state chemical transformation with phenolic and Mannich bridge structures as shown in Fig. 4(a). The chemical structures and thermal properties of OAVS-BZ HPP under thermal ROP were carefully characterized and investigated at different temperatures [from 25 to 300 °C] by using different techniques [DSC, TGA, FTIR, and solid-state NMR spectroscopy]. Fig. 4(b) displays DSC thermograms of OAVS-BZ HPP after thermal ROP. As mentioned previously, the uncuring of OAVS-BZ HPP displays a thermal ROP peak at 309 °C with corresponding enthalpies of 168 J g^{-1}. The thermal ROP peak was shifted to 302, 300, 298, and 296 °C with the thermal enthalpies of 157, 152, 149, and 99 J g^{-1} with an increase in the ROP temperature at 100, 150, 180, and 210 °C, respectively. As the thermal ROP temperature increased to 250 °C and 300 °C, at these temperatures, the thermal polymerization peak of OAVS-BZ HPP disappeared, indicating complete ring-opening polymerization of the oxazine ring. The results could be supported by FTIR spectra analyses as provided in Fig. 4(c), with the rise in thermal ROP temperature, the characteristic peaks of OAVS-BZ HPP at 937 cm^{-1} (oxazine ring) and 2100 cm^{-1} (C≡C bond) gradually lost their intensity and then totally disappeared as the thermal ROP temperature exceeding 250 °C, indicating successful thermal polymerization. The solid-state ^{13}C and ^{29}Si NMR spectra of OAVS-BZ HPP highlight key structural features. Before the thermal ROP process, the oxazine ring and C≡C units exhibit signals within the chemical shift range of 52.3–85.2 ppm in the solid-state ^{13}C NMR spectra as shown in Fig. 4(d). However, these signals vanish after thermal ROP, confirming the successful conversion of the functional groups and the formation of a robust ring-opening structure with phenolic and Mannich bridge structures (Fig. 4(a)). We also utilized solid-state ^{29}Si NMR to analyze the thermally ROP OAVS-BZ HPP. The results indicated that the characteristic ^{29}Si NMR patterns had also remained consistent with the similar positions after thermal ROP, verifying that the OAVS framework remains intact after ROP, as shown in Fig. 4(e). The changes in their corresponding thermal properties after thermal ROP were evaluated using TGA analyses as shown in Fig. 4(f). It was observed that after thermal ROP at 250 °C, the thermal degradation temperature was strongly overlapped at temperatures lower than

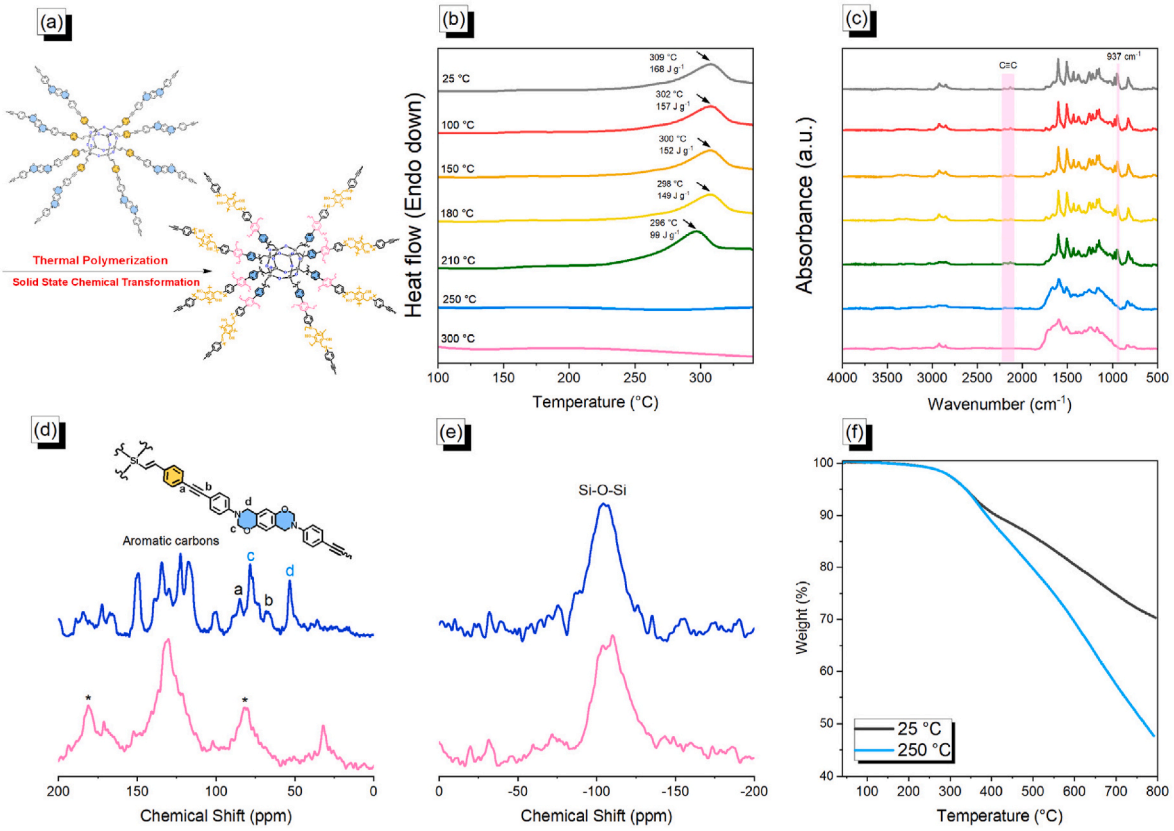

Fig. 4. (a) Solid state chemical transformation of OAVS-BZ HPP to poly(OAVS-BZ) HPP, (b) DSC thermal analyses, (c) in-situ FTIR spectral analyses, (d) ^{13}C NMR, (e) ^{29}Si NMR, and (f) TGA analyses.

375 °C; however, the carbon residue was strongly decreased from 70.3 % to 47.8 wt% [Table S1]. This reduction may be attributed to the formation of flexible aliphatic methylene (CH_2) units during thermal ROP, which reduces the rigidity and crosslinking density of OAVS-BZ HPP and then exhibits lower thermal stability [36,37]. This phenomenon is usually observed for the benzoxazine-based porous organic polymers after thermal ROP procedures in our previous studies, and this outcome differs from that of conventional low-molecular-weight benzoxazine monomers [36,37].

To evaluate the porosity characteristics of OAVS-BZ HPP during thermal ring-opening polymerization (ROP) for the formation of poly (OAVS-BZ) HPP, Fig. 5(a) presents the N_2 adsorption/desorption isotherm. With a SA_{BET} of 21.2 $m^2\ g^{-1}$, V_{total} of 0.14 $cm^3\ g^{-1}$, and an average pore diameter of approximately 2.36 nm, the material can potentially be classified as type I according to the IUPAC classification. The significantly reduced SA_{BET} of poly(OAVS-BZ) HPP relative to its OAVS-BZ HPP precursor is consistent with previous studies [36,37], which have demonstrated that the solid-state ring-opening polymerization (ROP) of benzoxazine units induces the formation of rigid structural motifs, such as Mannich bridges and densely hydrogen-bonded phenolic hydroxyl groups. These features contribute to the collapse of microporous domains and a consequent reduction in the overall surface area of the polymer network. The XRD pattern of poly (OAVS-BZ) HPP displays the broad amorphous peak at 21.6° as shown in Fig. 5(b), indicating the microporous amorphous feature with a hybrid porous polymer. Fig. 5(d) and (e) display TEM and SEM images of poly (OAVS-BZ) HPP, which both show the amorphous and disordered agglomerations. The EDX mapping (Fig. 5(f)–(i)) confirms that C, N, O, and Si atoms are evenly distributed throughout the poly(OAVS-BZ) HPP sample. Further elemental analyses can also be confirmed from XPS results (Fig. 5(c)), and the compositions were summarized in Table S2.

In Fig. 6(a), the disappearance of the C≡C peak and the peak at 937 cm^{-1} clearly confirms the occurrence of thermal ROP. The Si–*O*–Si peak at 1100 cm^{-1} verifies that the OAVS framework remains intact. Additionally, the originally sharp peak in the 1200-1800 cm^{-1} region becomes considerably broader after ROP, indicating structural transformation because of molecular mobility.

is restricted to poly(OAVS-BZ) HPP. Fig. 6(b)–(e) further examines the deconvoluted XPS peaks for C, N, O, and Si after thermal ROP. Following the thermal ROP, the C ≡C signal at 284.0 eV disappeared, and the C–Si peak shifted from its original 284.3 eV–284.0 eV. In addition, the binding energies for C=C, C–C, C–O, and C–N (284.9, 285.1, 285.6, and 286.6 eV, respectively) increased, indicating an enhancement in the corresponding bond strengths (Fig. 6(b)). However, the N_{1s} spectrum revealed a peak at 400.5 eV, which corresponds to the hydrogen bonding between the N–C bond and O–H groups formed after the oxazine ring opening in OAVS-BZ HPP (Fig. 6(c)). The appearance of an O–H signal in the O_{1s} spectrum of poly(OAVS-BZ) HPP confirms the successful opening of the oxazine (Fig. 6(d)). For Si_{2p}, minimal changes are observed; the characteristic peaks for Si–C and Si–O remain at 103.3 eV and 101.7 eV, respectively (Fig. 6(d)). Fig. 6(f) summarizes the elemental composition change before and after ROP. The changes in element ratios reflect the structural transformation during polymerization, and we could observe that the polar N, O, and even Si atom compositions were increased, which is an advantage for gas adsorption, especially in CO_2 capture ability.

3.4. CO_2 capture of the OAVS-BZ and Poly(OAVS-BZ) HPPs

The CO_2 adsorption capacity of OAVS-BZ HPP was measured as 16.0 and 23.1 $cm^3\ g^{-1}$ at 1 bar for 298, and 273 K; respectively. Although BET analyses of poly(OAVS-BZ) HPP after ROP show a decrease in both SA_{BET} and V_{total}, which would normally be unfavorable for CO_2 capture, the adsorption results indicate that poly(OAVS-BZ) HPP exhibits enhanced

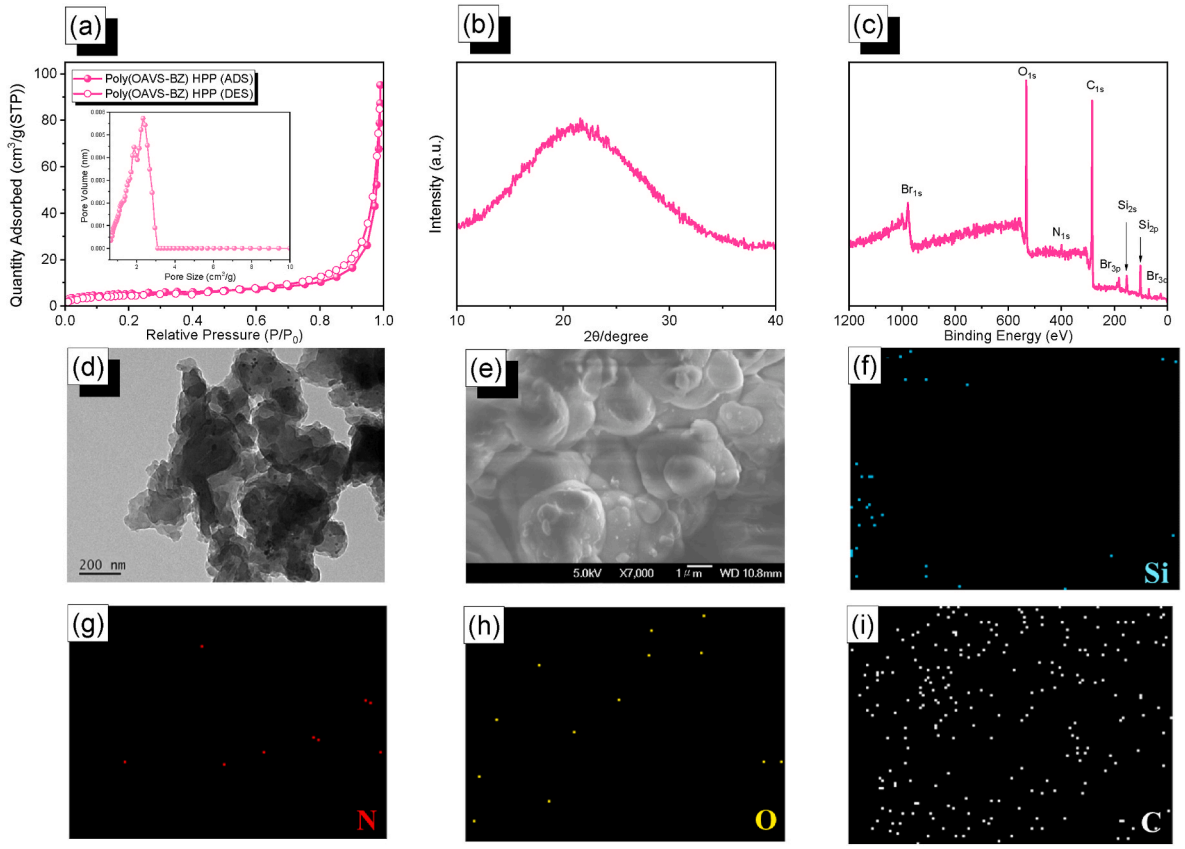

Fig. 5. (a) N_2 adsorption/desorption isotherms at 77 K and its corresponding pore size distribution and (b) Wide-angle X-ray diffraction pattern of poly(OAVS-BZ) HPP and the corresponding (c) XPS spectrum, (d) TEM, (e) SEM, and SEM-EDS analyses of (f) C, (g) N, (h) O, and (i) Si atoms of poly(OAVS-BZ) HPP.

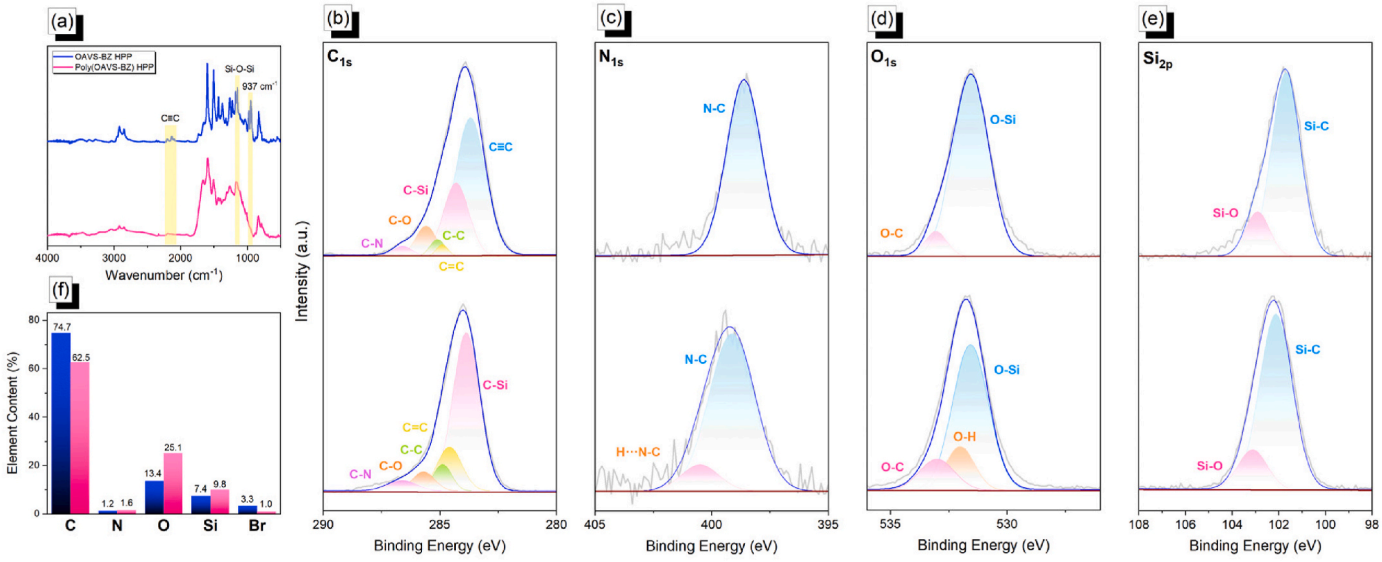

Fig. 6. (a) FTIR spectra of OAVS-BZ HPP and poly(OAVS-BZ) HPP and their corresponding curve fitting results of XPS spectra of (b) C_{1s}, (c) N_{1s}, (d) O_{1s}, (e) Si_{2p} (top: OAVS-BZ HPP, down: poly(OAVS-BZ) HPP after thermal ROP at 250 °C, (f) their corresponding element contents of OAVS-BZ HPP and poly(OAVS-BZ) HPP.

performance. Under the same conditions, its CO_2 adsorption capacities are 23.3 and 27.0 $cm^3\ g^{-1}$ at 298 and 273 K; respectively [Fig. 7(a) and (b)]. This improvement is attributable to the formation of abundant phenolic OH groups and nitrogen atoms on the surface following the solid-state chemical conversion, which improves CO_2 capture performance as confirmed by the XPS result. Fig. 7(c) illustrates the Q_{st} (isosteric heat of sorption) for CO_2 capture based on the Clausius-Clapeyron equation of OAVS-BZ and poly(OAVS-BZ) HPPs. It can offer insightful information on adsorption procedures. Clearly, the poly (OAVS-BZ) HPP is always greater than the OAVS-BZ HPP at all pressures, indicating that the poly(OAVS-BZ) HPP has stronger interaction with CO_2, such as hydrogen bonding and other reversible interactions, as shown in Fig. 7(d). Additionally, these functional groups increase the number of active sites, allowing more CO_2 molecules to be adsorbed.

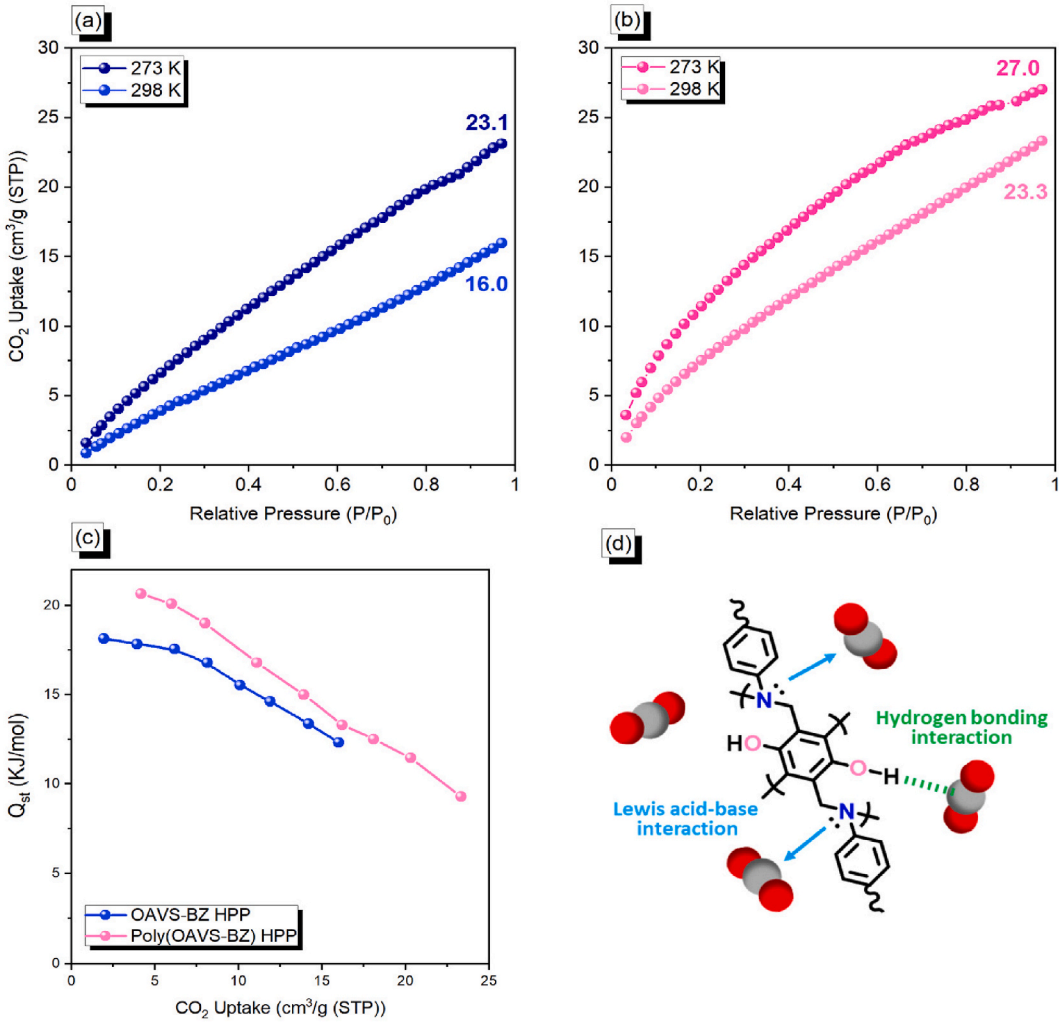

Fig. 7. CO_2 uptakes of (a) OAVS-BZ HPP and (b) poly(OAVS-BZ) HPP at 273 and 298 K, (c) isosteric heat of sorption at various CO_2 uptake capacities, and (d) the possible interactions of poly(OAVS-BZ) HPP with the CO_2 molecule.

They also create a favorable microenvironment within the pores through hydrogen bonding and acid-base interactions via [OH···O–C] or [N···C–O] interactions, further strengthening CO_2 adsorption [36,37,55,56,60–64]. Moreover, these conversion units contribute to the structural stability and optimization of pore size distribution, facilitating easier access and retention of CO_2 molecules. The triple bond structures, when converted into benzene rings, add significant aromaticity to the material. This transformation enhances CO_2 capture in several ways. The aromatic rings provide π-electron clouds that interact with the quadrupole moment of CO_2, promoting stronger π-π interactions. Furthermore, the conversion increases the overall structural rigidity, which can help maintain an optimal pore structure for gas adsorption. Thus, while the initial triple bonds offer reactivity, their transformation into benzene rings ultimately contributes to more efficient CO_2 capture by creating a more stable framework with enhanced active sites.

4. Conclusions

This study successfully synthesized a new hybrid porous polymer (HPP), OAVS-BZ HPP, through the Sonogashira–Hagihara coupling reaction between OAVS-8Br and DHTA-EA-BZ. The structural integrity of the synthesized OAVS-BZ HPP was confirmed using various spectroscopic techniques, including FTIR, NMR (^{1}H, ^{13}C, and ^{29}Si), and XPS, which demonstrated the effective incorporation of benzoxazine units onto the OAVS framework. The thermal properties of OAVS-BZ HPP were systematically analyzed using DSC and TGA, revealing its high thermal stability with a T_{d10} of 411 °C and high char yield of 70.3 wt%, which is higher than its precursor materials. The thermal ROP of OAVS-BZ HPP was investigated, showing a shift in exothermic peaks and a decrease in reaction enthalpy, indicative of structural transformation and the successful conversion of the oxazine rings into phenolic and Mannich bridge structures, which was further confirmed by FTIR and solid-state NMR analyses. Additionally, the porous properties of OAVS-BZ HPP were evaluated using N_2 adsorption/desorption isotherms, revealing a BET surface area of 43.5 $m^2\ g^{-1}$ and a microporous structure. After thermal ROP, a decrease in porosity and surface area was observed, but it can enhance the CO_2 capture capacity. As a result of hydrogen bonding and acid-base interactions with the CO_2 molecule, a high density of phenolic hydroxyl groups and nitrogen atoms has been generated on the surface. The CO_2 adsorption capacity increased from 16.0 to 23.3 $cm^3\ g^{-1}$ at 298 K under 1 bar, before and after the thermal ring-opening polymerization (ROP) of OAVS-BZ HPP, respectively. This study provides valuable insights into the structure-property relationships of POSS-based benzoxazine polymers and opens new possibilities for their application in advanced materials and gas adsorption.

CRediT authorship contribution statement

Ching-Wen Hsiao: Writing – original draft, Formal analysis, Data curation, Conceptualization. **Mohamed Gamal Mohamed:** Writing –

review & editing, Writing – original draft, Supervision, Methodology, Formal analysis, Data curation, Conceptualization. **Shiao-Wei Kuo:** Supervision, Resources, Project administration.

Declaration of competing interest

The authors declare that they have no known competing financial interests or personal relationships that could have appeared to influence the work reported in this paper.

Acknowledgments

This study was supported financially by the National Science and Technology Council, Taiwan, under contracts NSTC 113-2223-E-110-001- and 113-2221-E-110-012-MY3. The authors thank the staff at National Sun Yat-sen University for their assistance with the TEM (ID: EM022600) experiments.

Appendix A. Supplementary data

Supplementary data to this article can be found online at https://doi.org/10.1016/j.mtchem.2025.102795.

Data availability

The data that has been used is confidential.

References

[1] A. Alam, A. Hassan, R. Bera, N. Das, Silsesquioxane-based and triptycene-linked nanoporous polymers (STNPs) with a high surface area for CO_2 uptake and efficient dye removal applications, Mater. Adv. 1 (2020) 3406–3416, https://doi.org/10.1039/D0MA00672F.

[2] C.W. Hsiao, A.M. Elewa, M.G. Mohamed, S.W. Kuo, Highly stable hybrid porous polymers containing polyhedral oligomeric silsesquioxane (POSS)/Dibenzo [g, p] chrysene and Dibenzo [b, d] thiophene units for efficient Rhodamine B dye removal, Sep. Purif. Technol. 332 (2024) 125771, https://doi.org/10.1016/j.seppur.2023.125771.

[3] Y. Yan, H. Yang, H. Liu, Silsesquioxane-based fluorescent nanoporous polymer derived from a novel AIE chromophore for concurrent detection and adsorption of Ru^{3+}, Sensor. Actuator. B Chem. 319 (2020) 128154 https://doi.org/10.1016/j.snb.2020.128154.

[4] D. Zhang, J. Zeng, S. Zhu, H. Ma, X. Kang, L. Lou, Z. He, Effects of polyhedral oligomeric silsesquioxane and silicon microstructure on the electric-optical performance of polymer dispersed liquid crystals, Opt. Mater. 140 (2023) 113877, https://doi.org/10.1016/j.optmat.2023.113877.

[5] A. Kannan, C. Muthuraj, A. Mayavan, S. Gandhi, Multifaceted applications of polyhedral oligomeric silsesquioxane and their composites, Mater. Today Chem. 30 (2023) 101568, https://doi.org/10.1016/j.mtchem.2023.101568.

[6] Y. Liu, W. Yang, H. Liu, Azobenzene-functionalized cage silsesquioxanes as inorganic–organic hybrid, photoresponsive, nanoscale, building blocks, Chem. Eur J. 21 (2015) 4731–4738, https://doi.org/10.1002/chem.201406142.

[7] C.Y. Chen, M.G. Mohamed, W.C. Chen, S.W. Kuo, Construction of Ultrastable porous carbons materials derived from organic/inorganic double decker silsesquioxane (DDSQ) hybrid as a high-performance electrode for supercapacitor, Mater. Today Chem. 34 (2023) 101773, https://doi.org/10.1016/j.mtchem.2023.

[8] M.G. Mohamed, M.H. Elsayed, Y. Ye, M.M. Samy, A.E. Hassan, T.H. Mansoure, Z. Wen, H.H. Chou, K.H. Chen, S.W. Kuo, Construction of porous organic/inorganic hybrid polymers based on polyhedral oligomeric silsesquioxane for energy storage and hydrogen production from water, Polymers (Basel) 15 (2023) 182, https://doi.org/10.3390/polym15010182.

[9] Z. Chen, D. Wang, S. Feng, H. Liu, An imidazole thione-modified polyhedral oligomeric silsesquioxane for selective detection and adsorptive recovery of Au (III) from aqueous solutions, ACS Appl. Mater. Interfaces 13 (2021) 23592–23605, https://doi.org/10.1016/j.mtchem.2023.101773.

[10] A. Lee, S. Dubinsky, E. Tumarkin, M. Moulin, A.A. Beharry, E. Kumacheva, Multifunctional hybrid polymer-based porous materials, Adv. Funct. Mater. 21 (2011) 1959–1969, https://doi.org/10.1002/adfm.201002453.

[11] M.G. Mohamed, M.H. Elsayed, A.E. Hassan, A. Basit, I.M.A. Mekhemer, H.H. Chou, K.H. Chen, S.W. Kuo, Hybrid porous polymers combination of octavinylsilsesquioxane/pyrene with benzothiadiazole units for robust energy storage and efficient photocatalytic hydrogen production from water, ACS Appl. Polym. Mater. 6 (2024) 5945–5956, https://doi.org/10.1021/acsapm.4c00655.

[12] A. Basit, M.G. Mohamed, M. Ejaz, B.X. Su, H. Manzoor, S.W. Kuo, Boosting supercapacitor energy storage using microporous carbon derived from an octavinylsilsesquioxane and fluorenone-linked porous hybrid polymer, ACS Appl. Energy Mater. 7 (2024) 7505–7516, https://doi.org/10.1021/acsaem.4c01796.

[13] M.G. Mohamed, M.Y. Tsai, C.F. Wang, C.F. Huang, M. Danko, L. Dai, T. Chen, S. W. Kuo, Multifunctional polyhedral oligomeric silsesquioxane (POSS) based hybrid porous materials for CO_2 uptake and iodine adsorption, Polymers (Basel) 13 (2021) 221, https://doi.org/10.3390/polym13020221.

[14] M. Ejaz, M.G. Mohamed, S.U. Sharma, J.T. Lee, C.F. Huang, T. Chen, S.W. Kuo, An ultrastable porous polyhedral oligomeric silsesquioxane/tetraphenylthiophene hybrid as a high-performance electrode for supercapacitors, Molecules (Basel) 27 (2022) 6238, https://doi.org/10.3390/molecules27196238.

[15] M. Soldatov, H. Liu, Hybrid porous polymers based on cage-like organosiloxanes: synthesis, properties and applications, Prog. Polym. Sci. 119 (2021) 101419, https://doi.org/10.1016/j.progpolymsci.2021.101419.

[16] X. Ren, S. Kong, Q. Shu, M. Shu, Palladium nanoparticles supported on a porous organic polymer: an efficient catalyst for Suzuki-Miyaura and Sonogashira coupling reactions, Chin. J. Chem. 34 (2016) 373–380, https://doi.org/10.1002/cjoc.201500797.

[17] L. Cata, N. Terenti, C. Cociug, N.D. Hadade, I. Grosu, C. Bucur, Bogdan C. I. Parvulescu, M. Mazur, J. Cejka, Sonogashira synthesis of new porous aromatic framework-entrapped palladium nanoparticles as heterogeneous catalysts for Suzuki–Miyaura cross-coupling, ACS Appl. Mater. Interfaces 14 (2022) 10428–10437, https://doi.org/10.1021/acsami.1c24429.

[18] D. Wang, W. Yang, L. Li, X. Zhao, S. Feng, H. Liu, Hybrid networks constructed from tetrahedral silicon-centered precursors and cubic POSS-based building blocks via Heck reaction: porosity, gas sorption, and luminescence, J. Mater. Chem. A 1 (2013) 13549–13558, https://doi.org/10.1039/C3TA12324C.

[19] Y. Du, H. Liu, Cage-like silsesquioxanes-based hybrid materials, Dalton Trans. 49 (2020) 5396–5405, https://doi.org/10.1039/D0DT00587H.

[20] M. Ejaz, M.M. Samy, Y. Ye, S.W. Kuo, M.G. Mohamed, Design hybrid porous organic/inorganic polymers containing polyhedral oligomeric silsesquioxane/pyrene/anthracene moieties as a high-performance electrode for supercapacitor, Int. J. Mol. Sci. 24 (2023) 2501, https://doi.org/10.3390/ijms24032501.

[21] M.G. Mohamed, T.H. Mansoure, Y. Takashi, M.M. Samy, T. Chen, S.W. Kuo, Ultrastable porous organic/inorganic polymers based on polyhedral oligomeric silsesquioxane (POSS) hybrids exhibiting high performance for thermal property and energy storage, Microporous Mesoporous Mater. 328 (2021) 111505, https://doi.org/10.1016/j.micromeso.2021.111505.

[22] M.G. Mohamed, N.Y. Liu, A.F.M. El-Mahdy, S.W. Kuo, Ultrastable luminescent hybrid microporous polymers based on polyhedral oligomeric silsesquioxane for CO_2 uptake and metal ion sensing, Microporous Mesoporous Mater. 311 (2021) 110695, https://doi.org/10.1016/j.micromeso.2020.110695.

[23] M.G. Mohamed, S.W. Kuo, Progress in the self-assembly of organic/inorganic polyhedral oligomeric silsesquioxane (POSS) hybrids, Soft Matter 18 (2022) 5535–5561, https://doi.org/10.1039/D2SM00635A.

[24] X. Lin, Y.Y. Deng, Q. Zhang, D. Han, Q. Fu, Effect of POSS size on the porosity and adsorption performance of hybrid porous polymers, Macromolecules 56 (2023) 1243–1252, https://doi.org/10.1021/acs.macromol.2c02486.

[25] N. Ahmed, H. Fan, P. Dubois, X. Zhang, S. Fahad, T. Aziz, J. Wan, Nano-engineering and micromolecular science of polysilsesquioxane materials and their emerging applications, J. Mater. Chem. A 7 (2019) 21577–21604, https://doi.org/10.1039/C9TA04575A.

[26] S. Takase, T. Hamada, K. Okada, S. Mineoi, J. Ohshita, Polysilsesquioxane-containing thermally degradable groups for potential application as thermal insulation materials, ACS Appl. Polym. Mater. 5 (2023) 1390–1397, https://doi.org/10.1021/acsapm.2c01900.

[27] M.G. Mohamed, S.W. Kuo, Functional polyimide/polyhedral oligomeric silsesquioxane nanocomposites, Polymers (Basel) 11 (2019) 26, https://doi.org/10.3390/polym11010026.

[28] H.W. Chen, M.G. Mohamed, Y.C. Kao, W.C. Chen, K. Chiou, S.W. Kuo, Overcoming synthetic challenges in developing High-Performance polybenzoxazine from Diamine-Functionalized Double-Decker silsesquioxane (DDSQ) cage, Eur. Polym. J. 232 (2025) 113929, https://doi.org/10.1016/j.eurpolymj.2025.113929.

[29] M.G. Mohamed, S.W. Kuo, Functional silica and carbon nanocomposites based on polybenzoxazines, Macromol. Chem. Phys. 220 (2019) 1800306, https://doi.org/10.1002/macp.201800306.

[30] W.C. Chen, Z.Y. Chen, Y. Ba, B. Wang, G. Chen, X. Fang, S.W. Kuo, Double-Decker-shaped polyhedral silsesquioxanes reinforced epoxy/bismaleimide hybrids featuring high thermal stability, Polymers (Basel) 14 (2022) 2380, https://doi.org/10.3390/polym14122380.

[31] C.H. Chiang, M.G. Mohamed, W.C. Chen, M. Madhu, W.L. Tseng, S.W. Kuo, Construction of fluorescent conjugated polytriazole containing double-decker silsesquioxane: click polymerization and thermal stability, Polymers (Basel) 15 (2023) 331, https://doi.org/10.3390/polym15020331.

[32] W.C. Chen, Y.H. Tsao, C.F. Wang, C.F. Huang, L. Dai, T. Chen, S.W. Kuo, Main chain–type block copolymers through atom transfer radical polymerization from double-decker–shaped polyhedral oligomeric silsesquioxane hybrids, Polymers (Basel) 12 (2020) 465, https://doi.org/10.3390/polym12020465.

[33] G. Cheng, N.R. Vautravers, R.E. Morris, D.J. Cole-Hamilton, Synthesis of functional cubes from octavinylsilsesquioxane (OVS), Org. Biomol. Chem. 6 (2008) 4662–4667, https://doi.org/10.1039/B812140K.

[34] W. Chaikittisilp, A. Sugawara, A. Shimojima, T. Okubo, Hybrid porous materials with high surface area derived from bromophenylethenyl-functionalized cubic siloxane-based building units, Chem. Eur J. 16 (2010) 6006–6014, https://doi.org/10.1002/chem.201000249.

[35] B. Kiskan, Adapting benzoxazine chemistry for unconventional applications, React. Funct. Polym. 129 (2018) 76–88, https://doi.org/10.1016/j.reactfunctpolym.2017.06.009.

[36] M. Ejaz, M.G. Mohamed, S.W. Kuo, Solid state chemical transformation provides a fully benzoxazine-linked porous organic polymer displaying enhanced CO_2 capture and supercapacitor performance, Polym. Chem. 14 (2023) 2494–2509, https://doi.org/10.1039/D3PY00158J.
[37] M.G. Mohamed, T.C. Chen, S.W. Kuo, Solid-state chemical transformations to enhance gas capture in benzoxazine-linked conjugated microporous polymers, Macromolecules 54 (2021) 5866–5877, https://doi.org/10.1021/acs.macromol.1c00736.
[38] Q. Ma, X. Liu, H. Wang, Q. Zhuang, J. Qian, Construction of novel benzoxazine-linked covalent organic framework with antimicrobial activity via postsynthetic cyclization, Mater. Today Chem. 23 (2022) 100707, https://doi.org/10.1016/j.mtchem.2021.100707.
[39] M.M. Samy, M.G. Mohamed, T.H. Mansoure, T.S. Meng, M.A.R. Khan, C.C. Liaw, S. W. Kuo, Solid state chemical transformations through ring-opening polymerization of ferrocene-based conjugated microporous polymers in host–guest complexes with benzoxazine-linked cyclodextrin, J. Taiwan Inst. Chem. Eng. 132 (2022) 104110, https://doi.org/10.1016/j.jtice.2021.10.010.
[40] K. Zhang, M. Han, L. Han, H. Ishida, H. Resveratrol-based tri-functional benzoxazines: synthesis, characterization, polymerization, and thermal and flame retardant properties, Eur. Polym. J. 116 (2019) 526–533, https://doi.org/10.1016/j.eurpolymj.2019.04.036.
[41] X. Liu, Y. Zeng, R. Yang, Y. Yu, G. Zhan, P. Zuo, Q. Zhuang, Advanced design of novel benzoxazines via a materials genome approach, Mater. Today Chem. 42 (2024) 102376, https://doi.org/10.1016/j.mtchem.2024.102376.
[42] Y. Xu, S. Xu, S. Liu, G. Liu, G. Li, Y. Yang, Ultralight, shapeable, and superhydrophobic polyacrylonitrile/polybenzoxazine aerogel for high oil-water separation capacity, Mater. Today Chem. 38 (2024) 102058, https://doi.org/10.1016/j.mtchem.2024.102058.
[43] I. Tiwari, P. Sharma, L. Nebhani, Polybenzoxazine - an enticing precursor for engineering heteroatom-doped porous carbon materials with applications beyond energy, environment and catalysis, Mater. Today Chem. 23 (2022) 100734, https://doi.org/10.1016/j.mtchem.2021.100734.
[44] M. Ejaz, M.G. Mohamed, S.W. Kuo, Fluorescent benzoxazine–Perylene linked covalent organic polymer as a sensing probe for lead ions and 2,4,6-trinitrophenol, ACS Appl. Polym. Mater. 6 (2024) 9170–9179, https://doi.org/10.1021/acsapm.4c01514.
[45] M. Ejaz, M.G. Mohamed, W.C. Huang, Y.C. Kao, W.C. Chen, S.W. Kuo, Highly thermally stable polyhedral oligomeric silsesquioxane based on diacetal-functionalized polybenzoxazine nanocomposites, Eur. Polym. J. 223 (2025) 113649, https://doi.org/10.1016/j.eurpolymj.2024.113649.
[46] Y.C. Kao, Y.H. Ku, M.G. Mohamed, W.H. Su, S.W. Kuo, Microphase separation transformation in bio-based benzoxazine/phenolic/PEO-*b*-PCL diblock copolymer mixtures induced by transesterification reaction, Macromolecules 58 (2025) 585–600, https://doi.org/10.1021/acs.macromol.4c02072.
[47] B. Lochab, M. Monisha, N. Amarnath, P. Sharma, S. Mukherjee, H. Ishida, Review on the accelerated and low-temperature polymerization of benzoxazine resins: addition polymerizable sustainable polymers, Polymers (Basel) 13 (2021) 1260, https://doi.org/10.3390/polym13081260.
[48] M.G. Mohamed, M.M. Samy, T.H. Mansoure, C.-J. Li, W.-C. Li, J.-H. Chen, K. Zhang, S.-W. Kuo, Microporous carbon and carbon/metal composite materials derived from bio-benzoxazine-linked precursor for CO_2 capture and energy storage applications, Int. J. Mol. Sci. 23 (2022) 347, https://doi.org/10.3390/ijms23010347.
[49] C.W. Hsiao, A.M. Elewa, M.G. Mohamed, M.G. Kotp, M.M.C. Chou, S.W. Kuo, Designing strategically functionalized hybrid porous polymers with octavinylsilsesquioxane/dibenzo[g,p]chrysene/benzo[c]-1,2,5-thiadiazole units for rapid removal of Rhodamine B dye from water, Colloids Surf. A Physicochem. Eng. Asp. 699 (2024) 134658, https://doi.org/10.1016/j.colsurfa.2024.134658.
[50] D. Wang, S. Feng, H. Liu, Fluorescence-tuned polyhedral oligomeric silsesquioxane-based porous polymers, Chem. Eur J. 22 (2016) 14319–14327, https://doi.org/10.1002/chem.201602688.
[51] N. Yang, Y. Wang, S. Huang, X. Yan, Q. Yan, Frustrated Lewis Pair Meets polyhedral oligomeric silsesquioxane: water-tolerant hybrid porous networks for robust, efficient, and recyclable CO_2 catalysis, ACS Appl. Mater. Interfaces 17 (2025) 7894–7905, https://doi.org/10.1021/acsami.4c20670.
[52] D.X. Wang, L. Xue, L.G. Li, B. Deng, S.Y. Feng, H.Z. Liu, X. Zhao, Rational design and synthesis of hybrid porous polymers derived from polyhedral oligomeric silsesquioxanes via Heck coupling reactions, Macromol. Rapid Commun. 34 (2013) 861–866, https://doi.org/10.1002/marc.201200835.
[53] X. Guo, J. Rabeah, R. Sun, D. Wang, E. Mejía, Fluorescent hybrid porous polymers as sustainable heterogeneous photocatalysts for cross-dehydrogenative coupling reactions, ACS Appl. Mater. Interfaces 13 (2021) 42889–42897, https://doi.org/10.1021/acsami.1c12377.
[54] M.G. Mohamed, C.C. Chen, K. Zhang, S.W. Kuo, Construction of three-dimensional porous organic polymers with enhanced CO_2 uptake performance via solid-state thermal conversion from tetrahedral benzoxazine-linked precursor, Eur. Polym. J. 200 (2023) 112551, https://doi.org/10.1016/j.eurpolymj.2023.112551.
[55] M.G. Mohamed, W.C. Chang, S.W. Kuo, Crown ether- and benzoxazine-linked porous organic polymers displaying enhanced metal ion and CO_2 capture through solid-state chemical transformation, Macromolecules 55 (2022) 7879–7892, https://doi.org/10.1021/acs.macromol.2c01216.
[56] M.G. Mohamed, B.X. Su, S.W. Kuo, Robust nitrogen-doped microporous carbon via crown ether-functionalized benzoxazine-linked porous organic polymers for enhanced CO_2 adsorption and supercapacitor applications, ACS Appl. Mater. Interfaces 16 (2024) 40858–40872, https://doi.org/10.1021/acsami.4c05645.
[57] X. Sun, J. Li, W. Wang, Q. Ma, Constructing benzoxazine-containing porous organic polymers for carbon dioxide and hydrogen sorption, Eur. Polym. J. 107 (2018) 89–95, https://doi.org/10.1016/j.eurpolymj.2018.07.043.
[58] L. Li, S. Feng, H. Liu, Novel hybrid luminescent materials derived from multicarboxy cage silsesquioxanes and terbium ion, J. Ceram. Soc. Jpn. 123 (2015) 719–724, https://doi.org/10.2109/jcersj2.123.719.
[59] Y. Du, M. Ge, H. Liu, Porous polymers derived from octavinylsilsesquioxane by cationic polymerization, Macromol. Chem. Phys. 220 (2019) 1800536, https://doi.org/10.1002/macp.201800536.
[60] X. Yang, R.J. Rees, W. Conway, G. Puxty, Q. Yang, D.A. Winkler, Computational modeling and simulation of CO_2 capture by aqueous amines, Chem. Rev. 117 (2017) 9524–9593, https://doi.org/10.1021/acs.chemrev.6b00662.
[61] L. Hong, S. Ju, X. Liu, Q. Zhuang, G. Zhan, X. Yu, Highly selective CO_2 uptake in novel fishnet-like polybenzoxazine-based porous carbon, Energy Fuels 33 (2019) 11454–11464, https://doi.org/10.1021/acs.energyfuels.9b02631.
[62] M. Ejaz, M.G. Mohamed, Y.T. Chen, K. Zhang, S.W. Kuo, Porous carbon materials augmented with heteroatoms derived from hyperbranched biobased benzoxazine resins for enhanced CO_2 adsorption and exceptional supercapacitor performance, J. Energy Storage 78 (2024) 110166, https://doi.org/10.1016/j.est.2023.110166.
[63] M.G. Mohamed, C.C. Chen, M. Ibrahim, A.O. Mousa, M.H. Elsayed, Y. Ye, S.W. Kuo, Tetraphenylanthraquinone and dihydroxybenzene-tethered conjugated microporous polymer for enhanced CO_2 uptake and supercapacitive energy storage, JACS Au 4 (2024) 3593–3605, https://doi.org/10.1021/jacsau.4c00537.
[64] M.G. Mohamed, C.C. Chen, S.W. Kuo, Nitrogen and sulfur co-doped microporous carbon through benzo[c]-1,2,5-thiadiazole-functionalized benzoxazine-linkage porous organic polymer in CO_2 capture and energy storage, React. Funct. Polym. 214 (2025) 106286, https://doi.org/10.1016/j.reactfunctpolym.2025.106286.